Optics and Lasers in Engineering 181 (2024) 108352

Contents lists available at ScienceDirect

Optics and Lasers in Engineering

journal homepage: www.elsevier.com/locate/optlaseng

Wavefront error peak removal by carrier phase reconstruction technique for slope measurement type sensors

Vu-Hai-Linh Nguyen [a,b], Manh-The Nguyen [b], Hyug-Gyo Rhee [a,b,*], Young-Sik Ghim [a,b,*]

[a] Department of Science of Measurement, University of Science and Technology (UST), Daejeon 34113, Korea
[b] Length and Dimensional Metrology Group, Physical Metrology Division, Korea Research Institute of Standards and Science (KRISS), Daejeon 34113, Korea

ARTICLE INFO

Keywords:
Wavefront reconstruction
Wavefront sensor
Deflectometry
Slopes measurement
Truncation error

ABSTRACT

A robust and novel technique for wavefront retrieval from slope data is presented in this paper. A simple wavefront with stable error is used as a carrier wavefront for measurement data to wipe out the error peaks arising from high-order aberration wavefronts. Several numerical simulations were performed to examine its speed, accuracy, and noise immunity. The accuracy of the outcomes outperformed those of prior algorithms when reconstructing wavefronts with high order aberration. On the other hand, the proposed technique requires additional processing time because it has more tasks. A deformable mirror was then used as a sample for experiments and the results obtained from the developed deflectometry system were compared to those obtained from input data of deformable mirror to evaluate the capabilities of the approach in practice.

1. Introduction

Wavefront measurement plays a vital role in modern technology. As proof, wavefront sensors are commonly employed in various types of adaptive optics and ophthalmology applications because of their straightforward structure and operating principle [1–4]. A large numbers of surface metrology and inspection systems, such as lateral shearing interferometers and deflectometry, require the wavefront to be reconstructed in the final step to obtain the outcome [5–7]. From a mathematical point of view, those systems use a wavefront gradient-based measurement method. This integration process needs an algorithm to achieve the desired shape, based on its slopes.

Previously, wavefront derivatives were obtained from measurement systems. A mathematical process was conducted to obtain the wavefront shape, in a process called wavefront reconstruction [8]. Basically, there are two categories of retrieval algorithm, the modal and zonal methods [9]. The modal method requires orthogonal basis polynomials like Zernike polynomials or Legendre polynomials as a reference to decompose the measurement slopes [10,11]. The zonal method assumes the wavefront is a set of height values in a discrete geometry [12–14]. A relation between height values and slopes is created as a set of linear equations, and phase is directly estimated from measured derivative data using a least square method or an iterative technique.

Besides the two old geometry styles introduced by Fried [12] and Hudgin [13], Southwell is acknowledged as one of the most popular geometries because of its error propagation [15] and its configuration, where the vertical, horizontal slopes and phase points are laid on the same position [9] as shown in Fig. 1. However, the original Southwell geometry can only deal with low order aberrations, including tilt, astigmatism, defocus, coma, and its combination. When reconstructing higher order aberrations, truncation error and error peaks often appear [16–18].

In the past decade, several studies have been published to address those problems. Li et al. presented an algorithm which utilized the Taylor theorem to analyze and incorporate a greater quantity of gradient data in the x and y directions [16]. Pathak and Phan increased the number of slopes by adding diagonal derivatives into the integral equations [19,20]. Recently, Hui [18] and Linh [17] also improved the Southwell geometry to renew the estimated phase equation which is depicted in Fig. 1. The former proposed that we can enhance accuracy by using the curvature factor [21] along with diagonal and anti-diagonal slope values. On the other hand, the latter rearranged the classical Southwell's algorithm to yield a new estimated phase equation with better truncation errors and speed. Those approaches can reduce the high order aberration error generally, but in reconstruction error there are a lot of aberration orders, which have a significantly higher error than others. The error peak does not disappear.

In this paper, we propose a novel and simple approach to reduce the

* Corresponding authors.
E-mail addresses: hrhee@kriss.re.kr (H.-G. Rhee), young.ghim@kriss.re.kr (Y.-S. Ghim).

https://doi.org/10.1016/j.optlaseng.2024.108352
Received 18 March 2024; Received in revised form 29 April 2024; Accepted 27 May 2024
Available online 10 June 2024

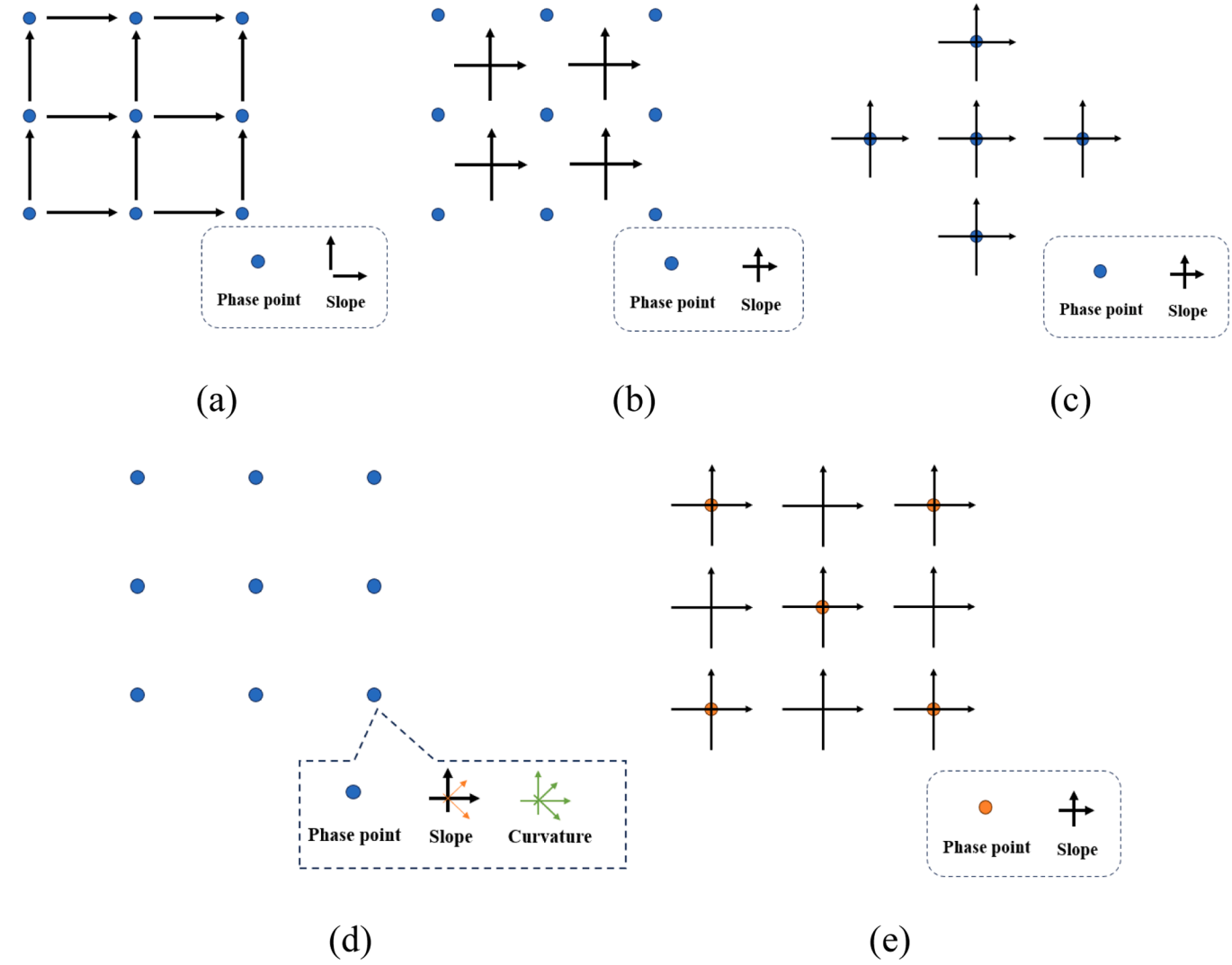

Fig. 1. Sampling geometry by: (a) Hudgin: slopes are lay on between 2 phase points, (b) Fried: slopes are measured at the center of the subaperture and are related to 4 phases at each corner, (c) Southwell: position of slopes and phase points are same, (d) Hui: Curvature factor was added, (e) Linh: additional slope and other phase points was used.

error peak problem of high order aberrations in a wavefront reconstruction algorithm which can be applied to all type of slope-based wavefront sensor such as: deflectometry, Shack-Hartmann wavefront sensor and lateral shearing interferometry. A simple wavefront was used as a carrier wavefront to easily remove the error peaks in all aberration orders. The remainder of this article is organized as follows. An explanation of error peaks and the principle of the carrier wavefront technique are given in Section 2. The numerical simulations and experimental results are provided in Section 3. Finally, discussion and conclusions are presented in Section 4.

2. Theory

2.1. Wavefront error peak definition

We start with an explanation of the wavefront error peak and its contribution to high order aberrations error.

To show the definition of error peak, we reconstruct wavefront with size of 500 × 500 by Linh algorithms. In Fig. 2(a), some wavefront shapes with peak are shown, and Fig. 2(b) presents its residual error distribution map after the reconstruction process. It is easy to see that the major errors are accumulated in the peak of the original surface. This phenomenon also happens in other algorithms when the surface has peaks, the slope around peaks area become high slope because of derivative definition. Thus, high slope areas will not be reconstructed perfectly. But we must note that not all wavefront aberrations have an error map distribution like Fig. 2(b). For example, Fig. 3 shows the phase map and the error distribution of function *xy*. It is apparent that the errors are really stable and small.

When we use the Zernike as a basis function to describe the distorted wavefront, it is obvious that there are some aberrations that have a greater number of peaks than the others in each order. For example, the radial order 3 of Zernike polynomials displayed in Fig. 4(a) have number of peak values are 3, 1, 1 and 3 respectively. On the other hand, the image illustrated in Fig. 4(b) tells us that the highest value areas of Zernike polynomials with radial order 4 are 4, 2, 1, 2, 4, respectively.

This is the reason why the relative reconstruction errors are not linear, as highlighted in Fig. 5. The quantity of peaks in the aberrations are not linear increasing corresponding the radial order of Zernike polynomials, then the error peak will appear in the relative error results.

2.2. Wavefront reconstruction by carrier wavefront technique

We start with a brief description of Southwell's geometry. As

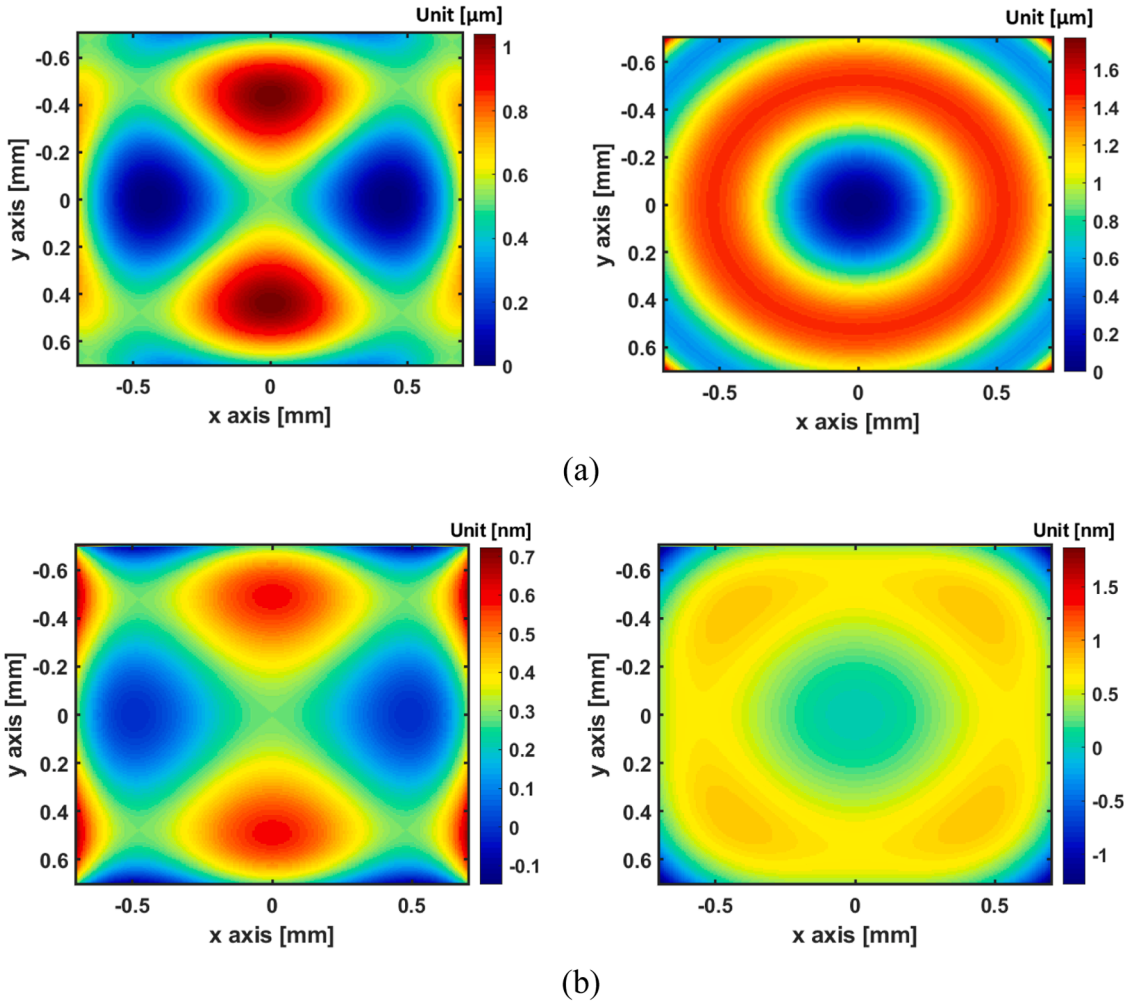

Fig. 2. (a) Some wavefront shapes with peak: Zernike polynomials Z_6^{-2} and Z_6^0. (b) Residual error of wavefront in Fig 2(a).

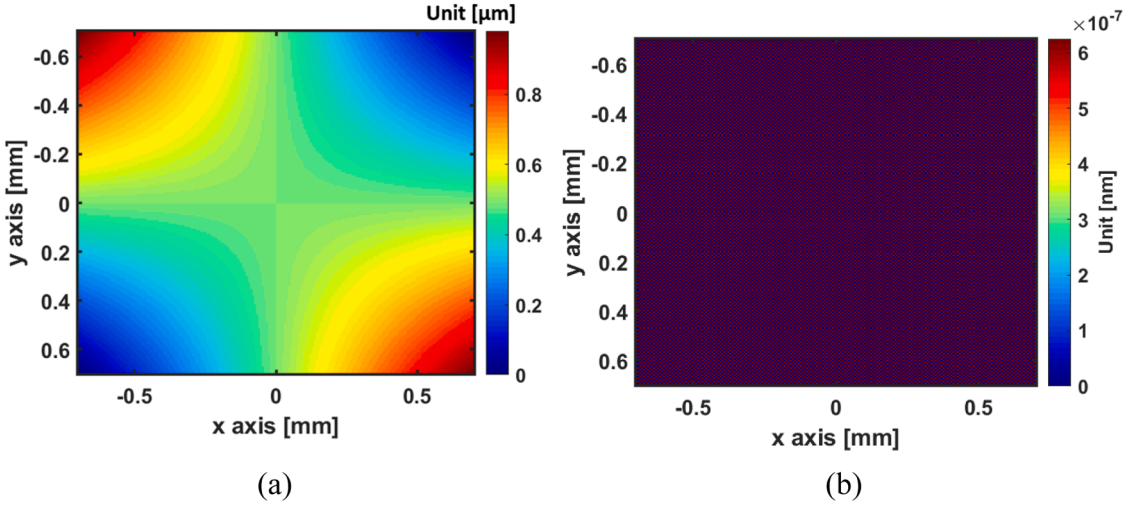

Fig. 3. (a) The phase map of wavefront *xy* and (b) Its residual errors.

illustrated in Fig. 6, the wavefront can be expressed as a set of phase points in grid geometry. Each of the nine points form a local domain. To reconstruct the height of the center point, Southwell's algorithm derives a relation between the height values and slope data of four surrounding points in the two orthogonal directions [9]:

$$\frac{W - W_4}{h} = \frac{S_x + S_{4x}}{2} \tag{1}$$

$$\frac{W_5 - W}{h} = \frac{S_{5x} + S_x}{2} \tag{2}$$

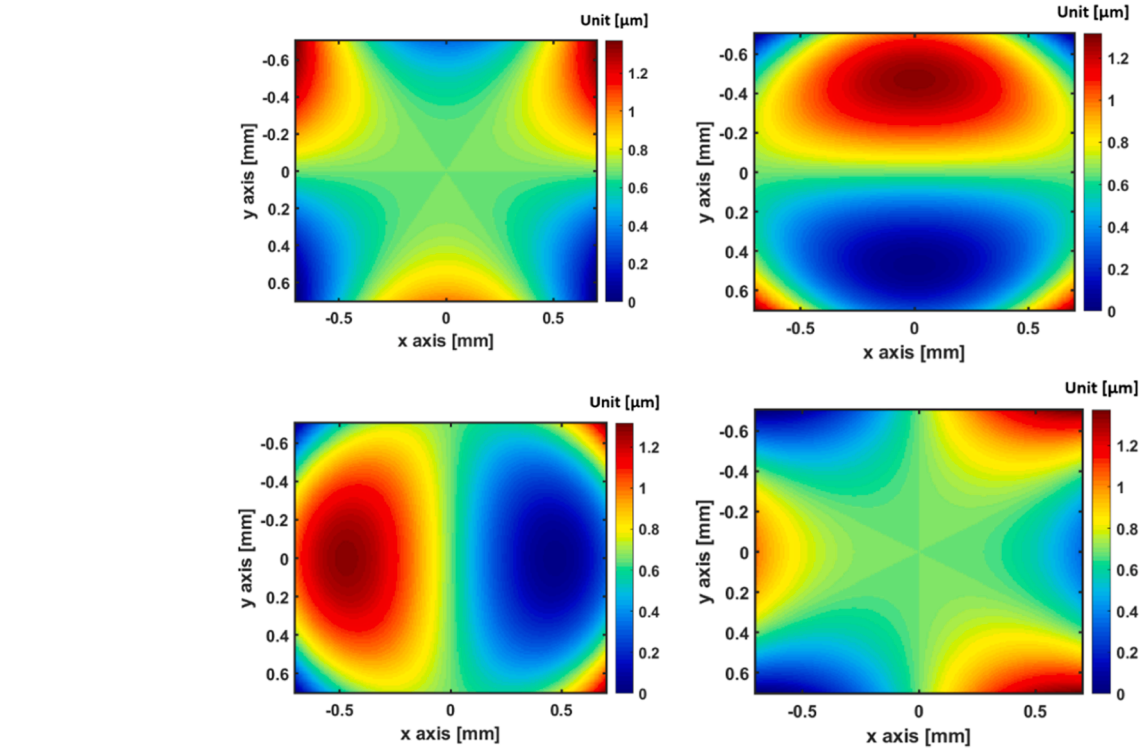

(a)

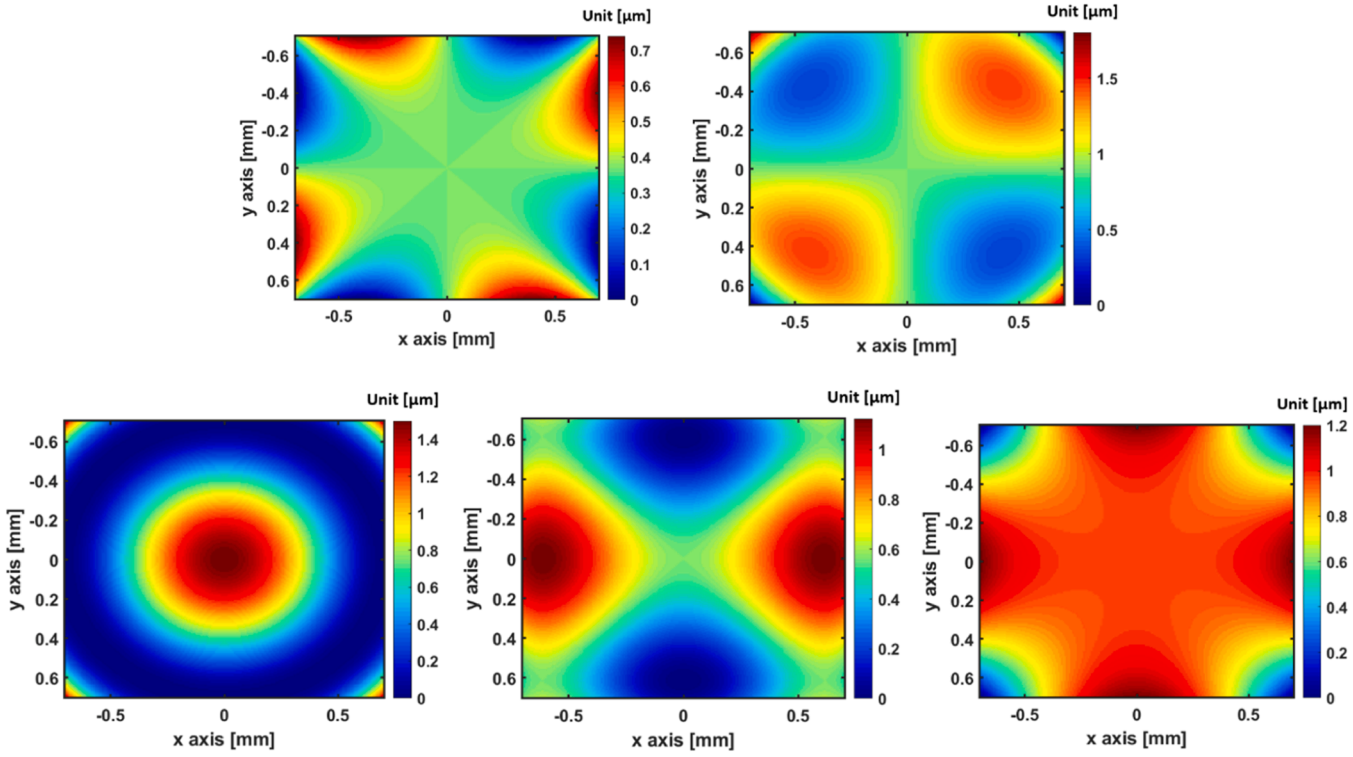

(b)

Fig. 4. Zernike polynomials with: (a) third radial order: Z_3^{-3}, Z_3^{-1}, Z_3^1 and Z_3^3 (b) fourth radial order: Z_4^{-4}, Z_4^{-2}, Z_4^0, Z_4^2 and Z_4^4 .

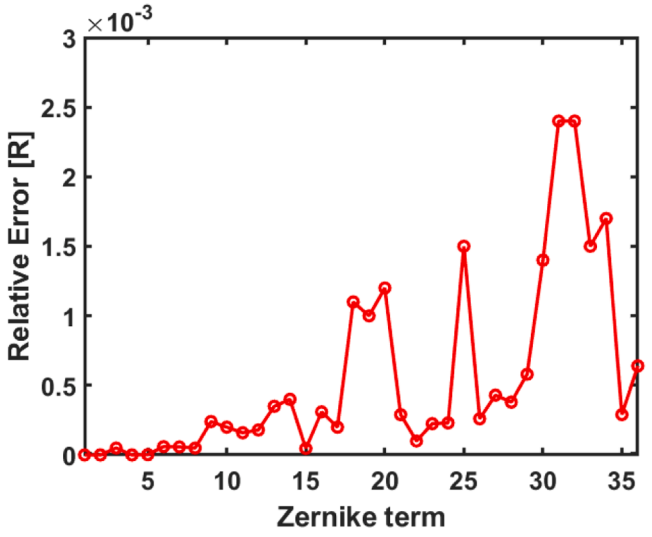

Fig. 5. The relative error levels of first 36 term Zernike polynomials.

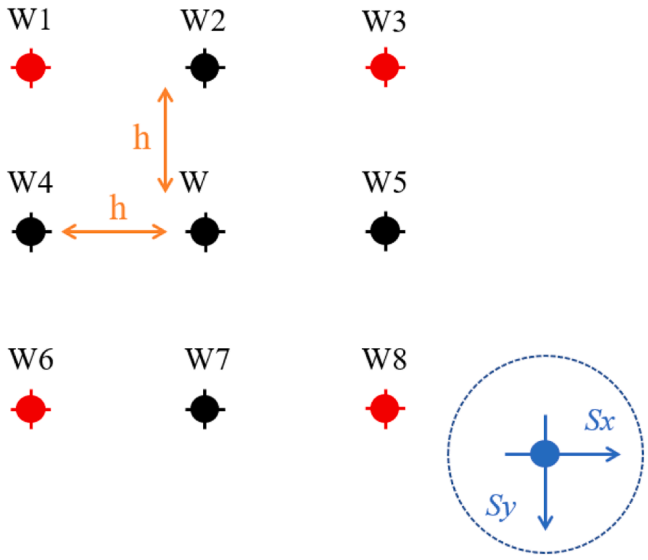

Fig. 6. Grid geometry for Zonal algorithms.

$$\frac{W - W_2}{h} = \frac{S_y + S_{2y}}{2} \tag{3}$$

$$\frac{W_7 - W}{h} = \frac{S_{7y} + S_y}{2} \tag{4}$$

where, W and S are the height values and slopes of phase points, respectively and h is distance between two phase points.

Thus, the estimated phase equation can be written as follows [9]:

$$f(W) = \frac{W_4 + W_5 + W_2 + W_7}{4} + \frac{h}{8} \times \left(S_{4x} - S_{5x} + S_{2y} - S_{7y}\right) \tag{5}$$

In Linh's modified version, the integral equation is expressed as follow [17]:

$$f(W) = \frac{W_1 + W_3 + W_6 + W_8}{4} + \frac{h}{16} \times \left(2S_{4x} - 2S_{5x} + 2S_{2y} - 2S_{7y} - S_{8x} - S_{8y} + S_{1x} + S_{1y} - S_{3x} + S_{3y} + S_{6x} - S_{6y}\right). \tag{6}$$

To reconstruct the original wavefront, we use an iterative technique to solve Eq. (6). For best performance, the successive over-relaxation (SOR) is performed [22]. Firstly, if the form of equation is written as [9]:

$$x_{n+1} = f(x_n), \tag{7}$$

we can obtain the SOR solution [9]:

$$x_{n+1}^{SOR} = (1 - \omega)x_n^{SOR} + \omega f\left(x_n^{SOR}\right), \tag{8}$$

where ω is the optimal relaxation factor [9]:

$$\omega = \frac{2}{1 + \sin[\pi/(N+1)]} \tag{9}$$

By Taylor theorem, the Eq. (6) can be expressed as [17]:

$$f(W) = \frac{(W_1 + W_3 + W_6 + W_8)}{4} + \frac{h}{16} \times \left(2S_{4x} - 2S_{5x} + 2S_{2y} - 2S_{7y} - S_{8x} - S_{8y} + S_{1x} + S_{1y} - S_{3x} + S_{3y} + S_{6x} - S_{6y}\right) + \frac{1}{48}O(h^4) + \ldots \tag{10}$$

Eq. (10) gives us the truncation error in slopes-based wavefront reconstruction process is $\frac{1}{48}O\left(h^4\right)$. Thus, when the original surface is a high order equation, the error will increase, especially for the order bigger than 4. In addition, when the surface has peaks, the slope around peaks area becomes high slope because of derivative definition. Approximation surface area with high slope always has bigger error than other parts. Therefore, our idea is reducing the high slope by adding some amount to original slope to change it to lower order function which we call carrier wavefront. Moreover, the height of slope especially in peak area also decreases following the form of selected carrier wavefront.

In this study, we will use this iterative zonal method to execute our idea. The details of our proposal are provided in Fig. 7.

We will select the function xy as a carrier wavefront W_c for two reasons. Firstly, its stable reconstruction error because the order of this function is smaller than 4. Secondly, there are no peaks found in the error distribution map of this function, as shown in Fig. 3.

S_x, S_y are our input slope measurement data. Then, we normally reconstruct the data to obtain the first reconstruction wavefront W:

$$f(W) = (1 - \omega)W_n^{SOR} + \omega f\left(W_n^{SOR}\right), \tag{11}$$

The wavefront adding amount W_a can be calculated as Eq. (12).

$$W_a = W_c - W, \tag{12}$$

After achieving W_a, its slopes are numerically attained as S_{ax}, S_{ay}, which is shown in Fig. 8 and Eq. (13), (14).

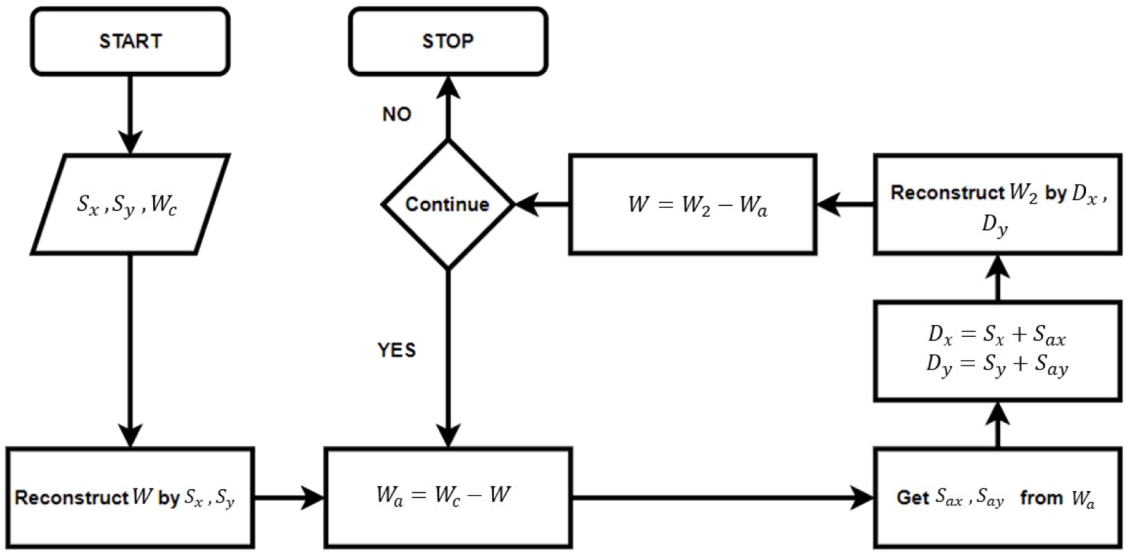

Fig. 7. Flow chart of our proposed algorithm.

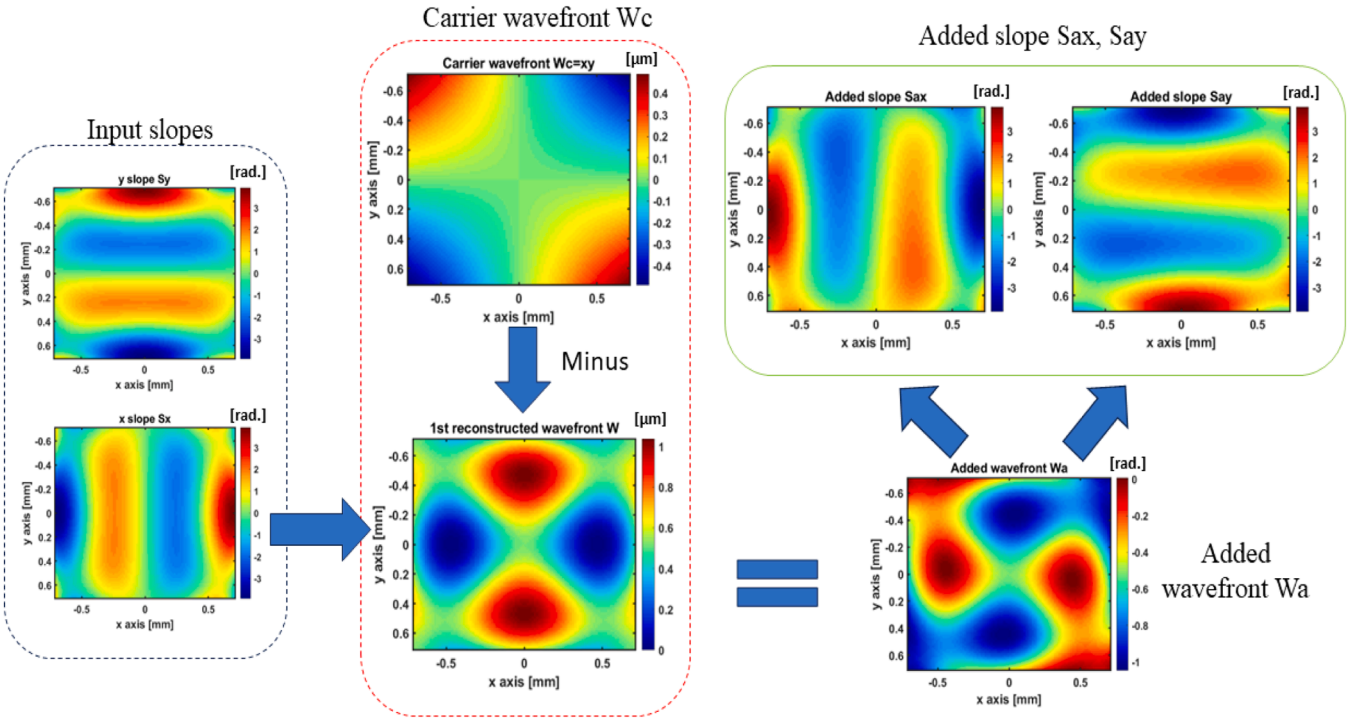

Fig. 8. Proposed algorithm procedure 1: Added slope S_{ax}, S_{ay} is calculated from carrier wavefront W_c and 1st reconstructed wavefront W.

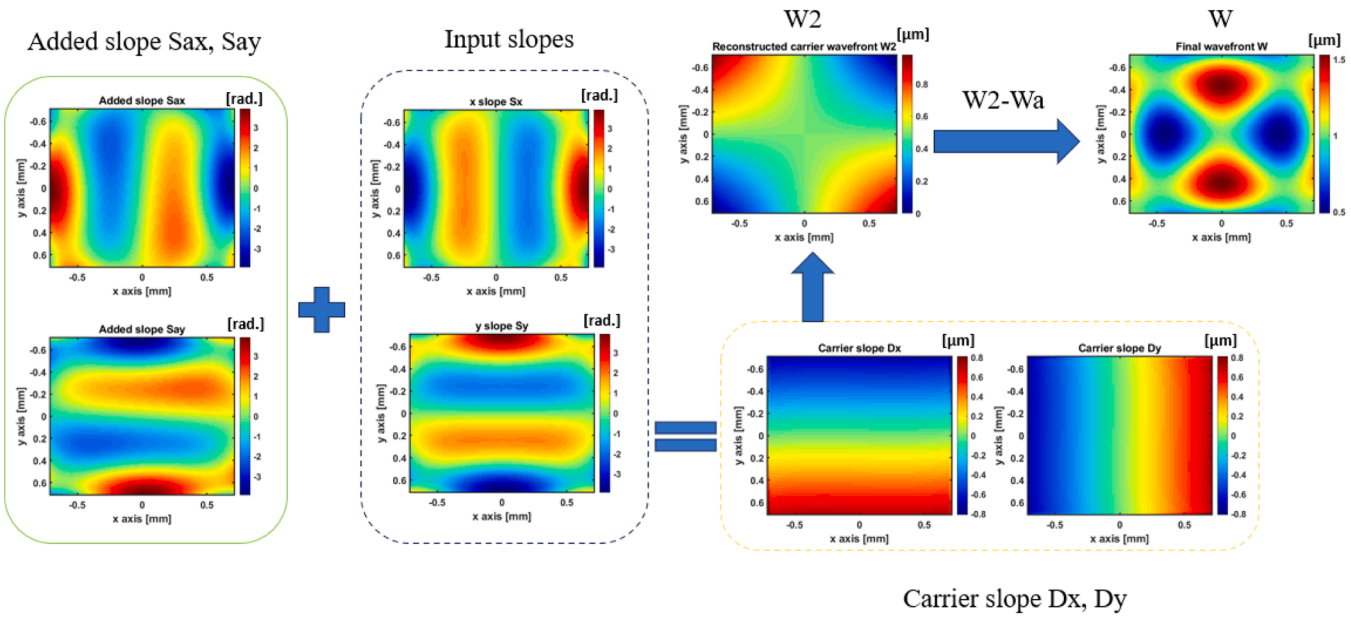

Fig. 9. Proposed algorithm procedure 2: Carrier wavefront slope D_x, D_y is estimated by sum of original slope S_x, S_y and added slope S_{ax}, S_{ay}, then final wavefront is extracted from difference between reconstructed carrier wavefront W_2 and added wavefront W_a.

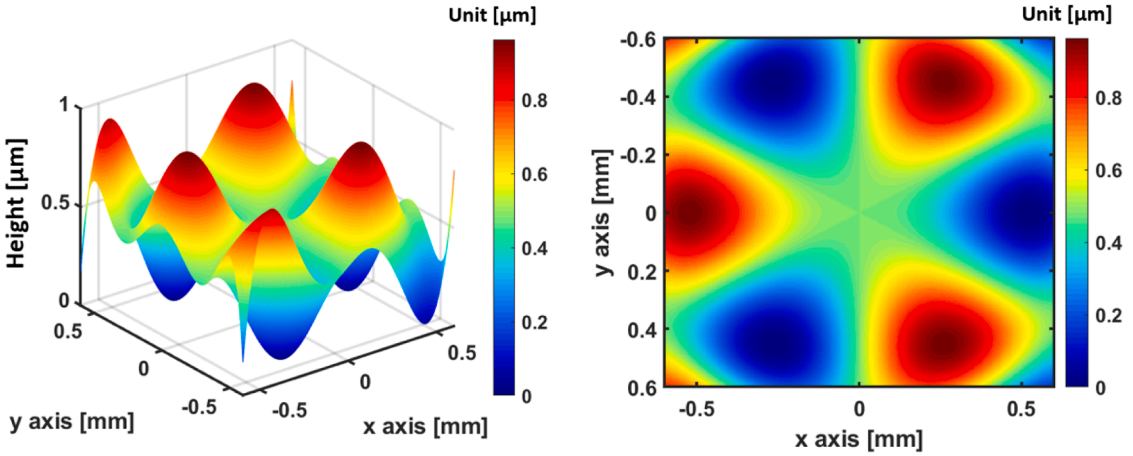

Fig. 10. The sample wavefront for simulation.

$$S_{ax} = \frac{dW_a}{dx}, \tag{13}$$

$$S_{ay} = \frac{dW_a}{dy}, \tag{14}$$

S_{ax}, S_{ay} can be used to estimate the carrier wavefront slope D_x, D_y as shown in Eq. (15) and (16).

$$D_x = S_x + \frac{dW_a}{dx}, \tag{15}$$

$$D_y = S_y + \frac{dW_a}{dy}, \tag{16}$$

From Fig. 9 we can see that slope D_x, D_y is smooth and no high slope appearing, this can be explained that D_x and D_y now are almost similar slope of carrier wavefront xy. In the last step, the wavefront W_2 is reconstructed before subtracting the added amount W_a, to receive the final reconstructed wavefront as illustrated in Fig. 9. At this point, we can even continue the algorithm loop to improve the results.

3. Simulation and experiment results

3.1. Numerical simulation

The focus of this section is to verify the performance of the proposed algorithm.

Initially, we used the original wavefront shape presented in Eq. (17) as a sample to define the distorted wavefront.

$$W = -10x^3 + 30xy^2 + 30x^5 - 60x^3y^2 - 90xy^4 - 21x^7 + 21x^5y^2 + 105x^3y^4 + 63xy^6 \tag{17}$$

The wavefront shape was demonstrated in Fig. 10 with clear peaks.

We will use 2 kinds of algorithms to examine the accuracy of the proposed technique. Firstly, we reconstruct the wavefront in Eq. (17) using the method proposed by Linh and apply our idea to the Linh algorithm. Fig. 11(a) is the residual error of the Linh algorithm and Fig. 11 (b) is the outcome when we apply the proposed idea.

The findings indicate that the peak of the residual error disappeared in the central area from Fig. 11(b), and the maximum error level was also improved, from 1.5 nm to 2 $\times 10^{-3}$ nm.

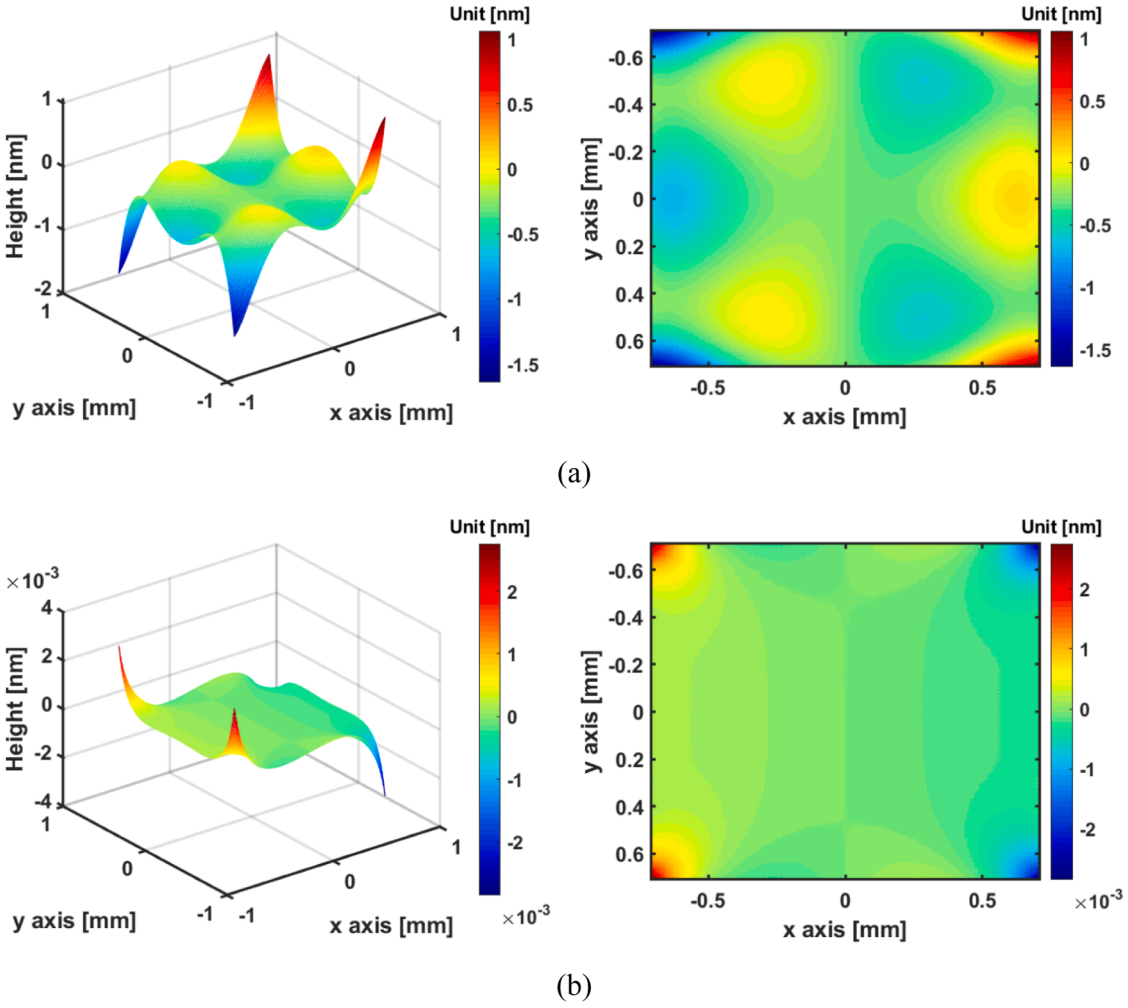

Fig. 11. (a) Residual error of Linh method. (b) Residual error of Linh method after applying proposed algorithm.

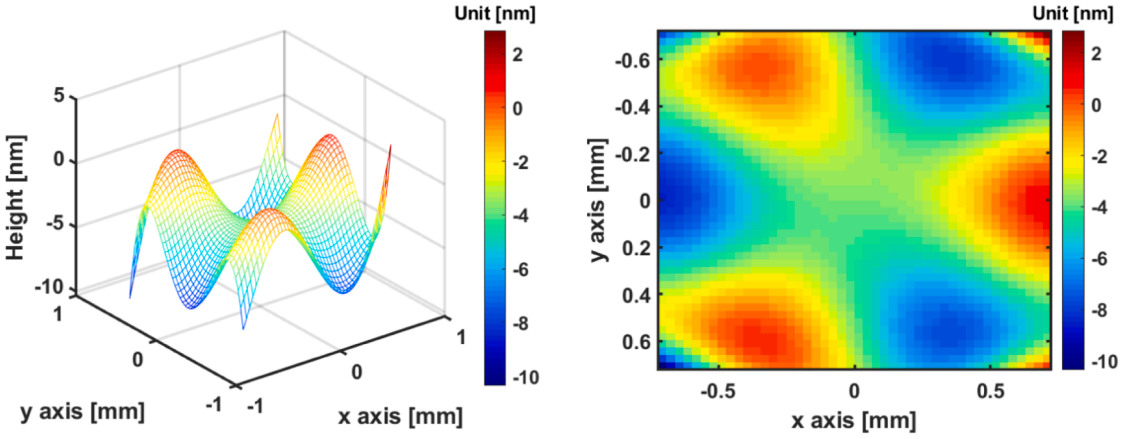

(a)

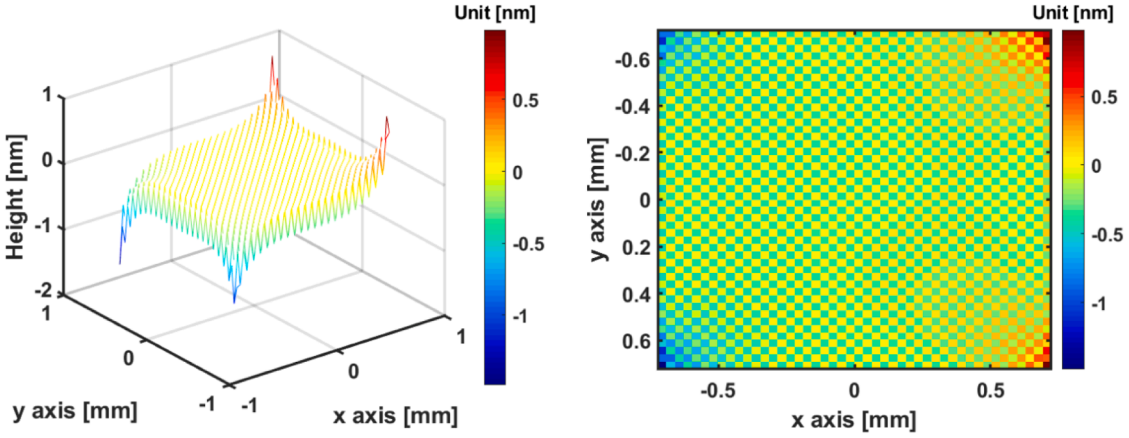

(b)

Fig. 12. (a) Residual error of Hui method. (b) Residual error of Hui method after applying proposed algorithm.

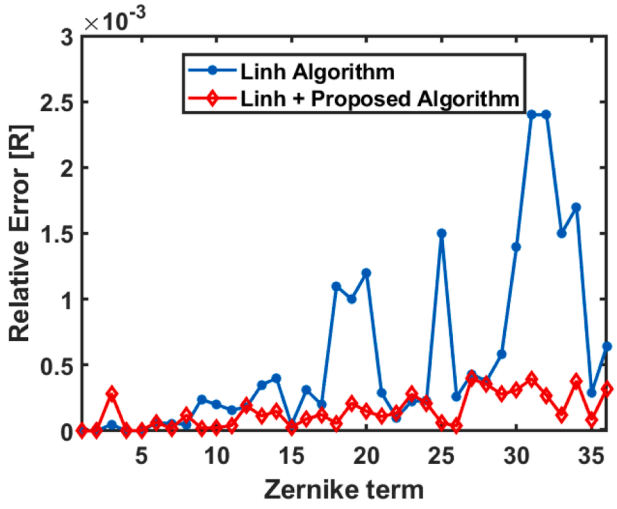

(a)

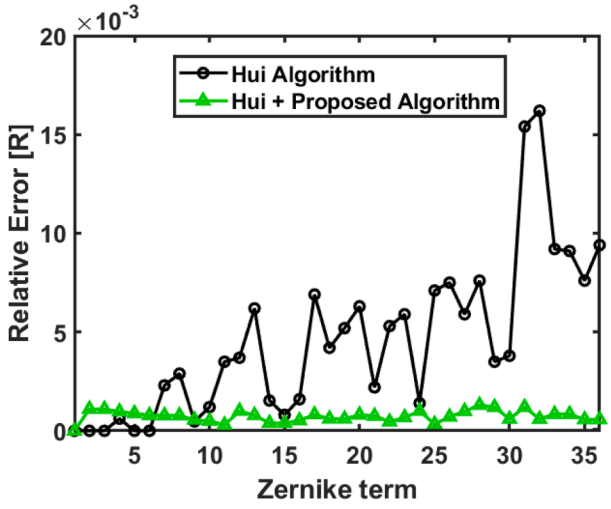

(b)

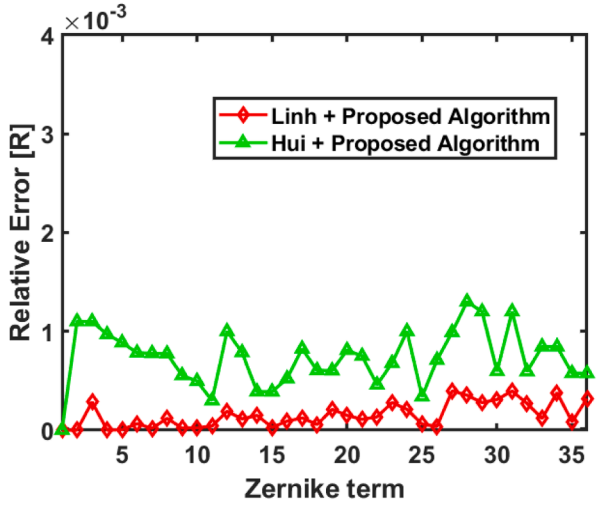

(c)

Fig. 13. Comparison of the relative error (a) Linh algorithm and Linh algorithm after using our method. (b) Hui algorithm and Hui algorithm after using our method. (c) Linh algorithm and Hui algorithm after using our method.

In the next simulation we also try to apply the proposed method to another type of algorithm. We select one least-square method from Hui as the reference. According to the data collected in Fig. 12(a) and (b), the error peak was also removed successfully, and the maximum error level was reduced from 10 nm to 1.5 nm. From the information gathered, our research is compatible with both an iterative method like the Linh algorithm and a least-square method like the Hui algorithm.

Next, we examine the peak removable efficiency of an algorithm in the Zernike order. We utilize the Zernike basis functions numbered by Noll [23] as a representative set to describe the sample wavefront. The order of the Zernike polynomial set is directly proportional to the degree of optical aberrations [24]. In our simulation, we employ the first 36 Zernike terms with 200 × 200 sampling points and the x, y range from $-\frac{\sqrt{2}}{2}$ to $\frac{\sqrt{2}}{2}$. These results are presented in Fig. 13. To compare the accuracy of the algorithms, we have estimated the relative root mean square error R [16]. R is defined as:

$$R = [\Delta W/W]^{1/2}, \tag{18}$$

where W is the original sample wavefront and ΔW is the estimated wavefront residual error.

As depicted in Fig. 13(a), the Linh algorithm exhibits a significant increase in relative errors as the order of the Zernike terms is raised, and some error peaks are found on each radial order of Zernike polynomials. On the other hand, after using the proposed algorithm the error remains linear, and it also drops sharply for the higher Zernike terms. For some very simple low aberrations such as tilt, using the proposed method did not outperform the conventional results, because its errors were always small. A matching situation occurred in Fig. 13(b) for the results of the Hui algorithm. We observed a desirable outcome when the error was much smaller and stable for increasing Zernike radial orders.

However, speed is a disadvantage of the proposed method. To estimate the speed of the algorithm, we used an iterative algorithm such as the Linh algorithm as a reference because of its rapidity and accuracy, even with a low performance computer. The information pertaining to this result is presented in Fig. 14.

According to Fig. 14, it is evident that the speed of the proposed method is significantly slower compared to the previous algorithm. For instance, with iterative method while the previous method took approximately 1.7 s to complete the reconstruction process for a 300 × 300 pixel wavefront, our algorithm required approximately 4 s. And by least square method our method costs 10.6 s while the previous method took about 5.56 s to reconstruct the 300 × 300 pixel wavefront. This disparity in results can be attributed to the fact that our proposed idea involves additional steps compared to the previous algorithm.

$$S_x = S_x + \alpha P \times S_x, \tag{19}$$

$$S_y = S_y + \alpha P \times S_y, \tag{20}$$

where: P is percentage of input noise and α is a random number belongs to $[-1, 1]$.

To examine the impact of noise on the reconstruction algorithm's sensitivity, we applied Gaussian distribution random noise as Eq. (19) and (20) ranging from 0 % to 16 % to the original wavefront slopes before the reconstruction process. The findings, presented in Fig. 15(a), (b) demonstrate that our proposed method has better noise resistance than the previous method, even with added noise. Nevertheless, when the level of noise surpassed approximately 10 %, the outcomes become uncertain. This phenomenon is easily understood because of 10 % Gaussian error is big for reconstruction the surface.

Furthermore, we also examine the noise resistance ability of proposed algorithm for Zernike surface sample. In this simulation we applied 8 % Gaussian distribution random noise to slope of Zernike term number 3, 6, 9, 14, 25 and 32 which are major influenced by error peaks corresponding to radial order from 1 to 6. The results were seen in

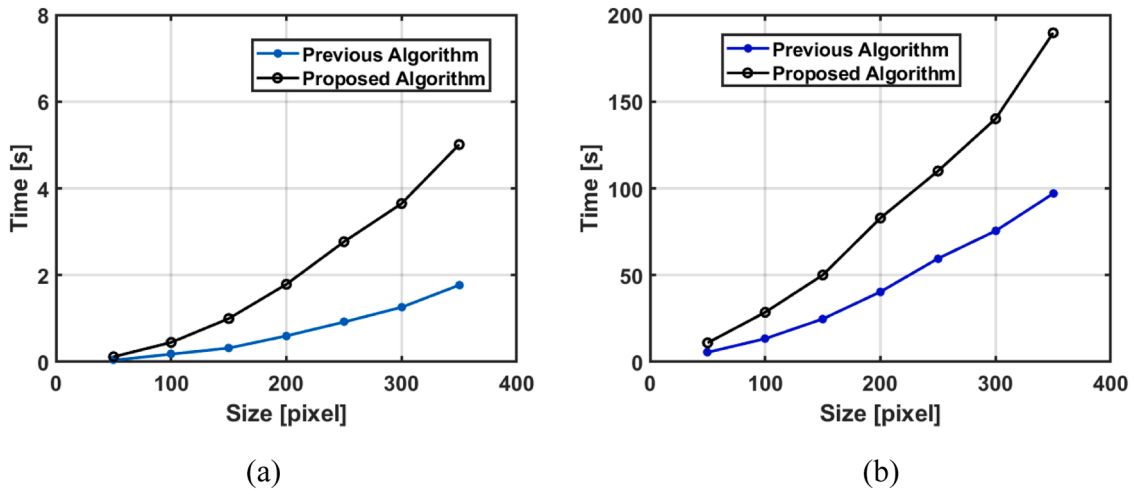

Fig. 14. Speed comparison of (a) Linh algorithm before and after using proposed method and (b) Hui algorithm before and after using proposed method.

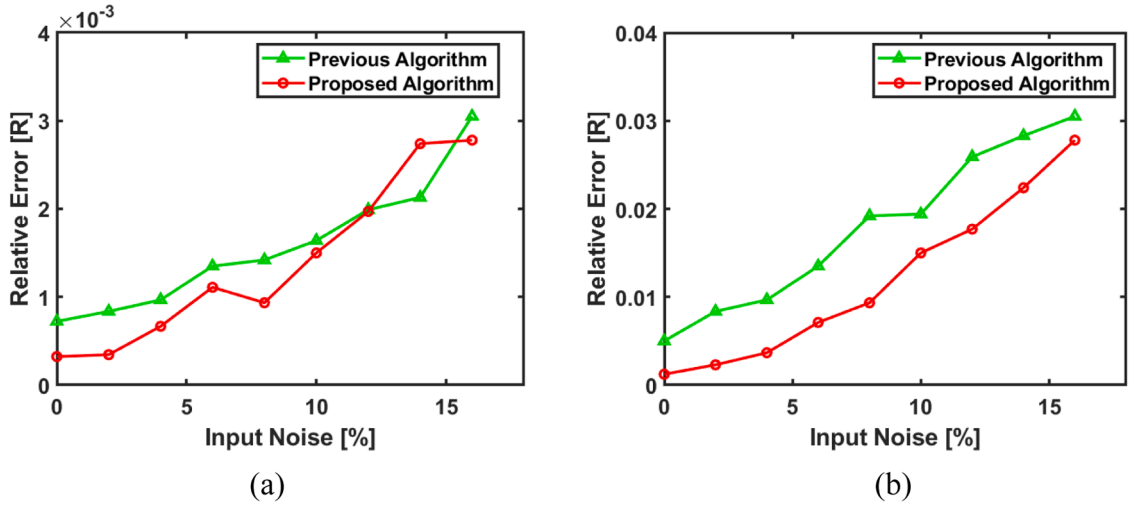

Fig. 15. Noise comparison of (a) Linh algorithm before and after using proposed method and (b) Hui algorithm before and after using proposed method.

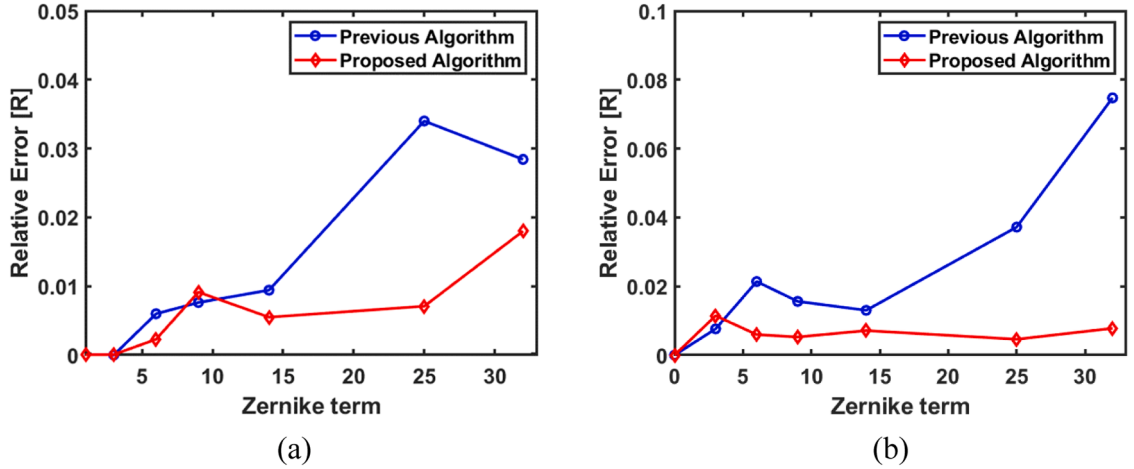

Fig. 16. Noise comparison of (a) Linh algorithm before and after using proposed method and (b) Hui algorithm before and after using proposed method for Zernike terms with order from 1 to 6.

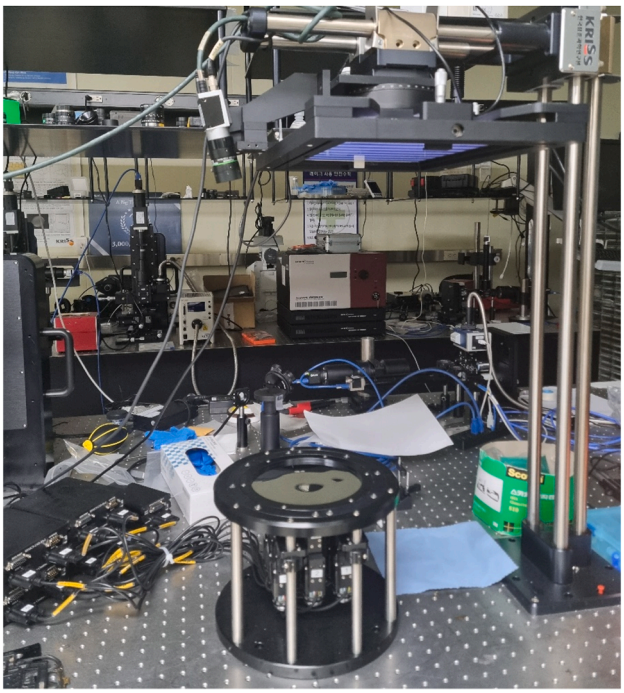

(a)

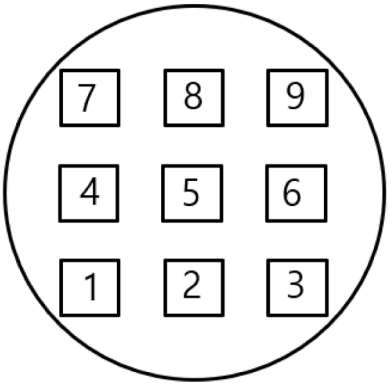

(b)

Fig. 17. (a) Deformable mirror and our deflectometry in the experiment (b) Actuator position of deformable mirror.

Fig. 16.

From Fig. 16(a) and (b) we can see that, although the relative error has an increasing trend in higher order, the proposed technique still can reduce the error in high order Zernike terms if compared to previous Linh algorithm.

3.2. Experimental results

To analyze the effectiveness of our algorithm, we measured the slopes of a deformable mirror using a deflectometry system as shown in Fig. 17 and compared the results to our input data of deformable mirror. Fig. 18 illustrates the concept of our deflectometer and the corresponding slope output.

A deflectometry system operates by creating sinusoidal fringe patterns in both horizontal and vertical axes through a computer. These patterns are displayed on a screen and projected onto the measurand. A camera captures the reflected images from the surface of the target. By utilizing additional information obtained from the calibration process, the local slopes of the surface of the target can be determined, as demonstrated in Fig. 18. In this experiment, deformable mirror was put 850 mm away from the screen and camera to capture good enough quality fringe pattern. we use a 1024 $\times$ 768 pixel resolution LCD with pixel size 0.24 mm. The used camera in this prototype is 2448 $\times$ 2048 pixel Basler acA2440–20 gm. with the pixel pitch of 3.45 μm. A pattern with frequency of 0.5 mm^{-1} was used in the LCD screen, the resolution of camera is 3.45 μm which is fair enough to prevent Moire patterns appearing when frequency in the LCD exceeds the pixel pitch of camera. The actuator 5 of deformable mirror was controlled to move 72 μm from original position. After that, inputting these slope data from the deflectometry in Fig. 18 into the proposed algorithm, the reconstructed surface of deformable mirror with our proposed method can be obtained, as shown in Fig. 19(a):

Fig. 19(a) and (b) provides us the results of the reconstructed surface of the deformable mirror, which was measured using deflectometry system and process by our proposed method and Linh algorithm, respectively. We can clearly realize the effective results of our method in

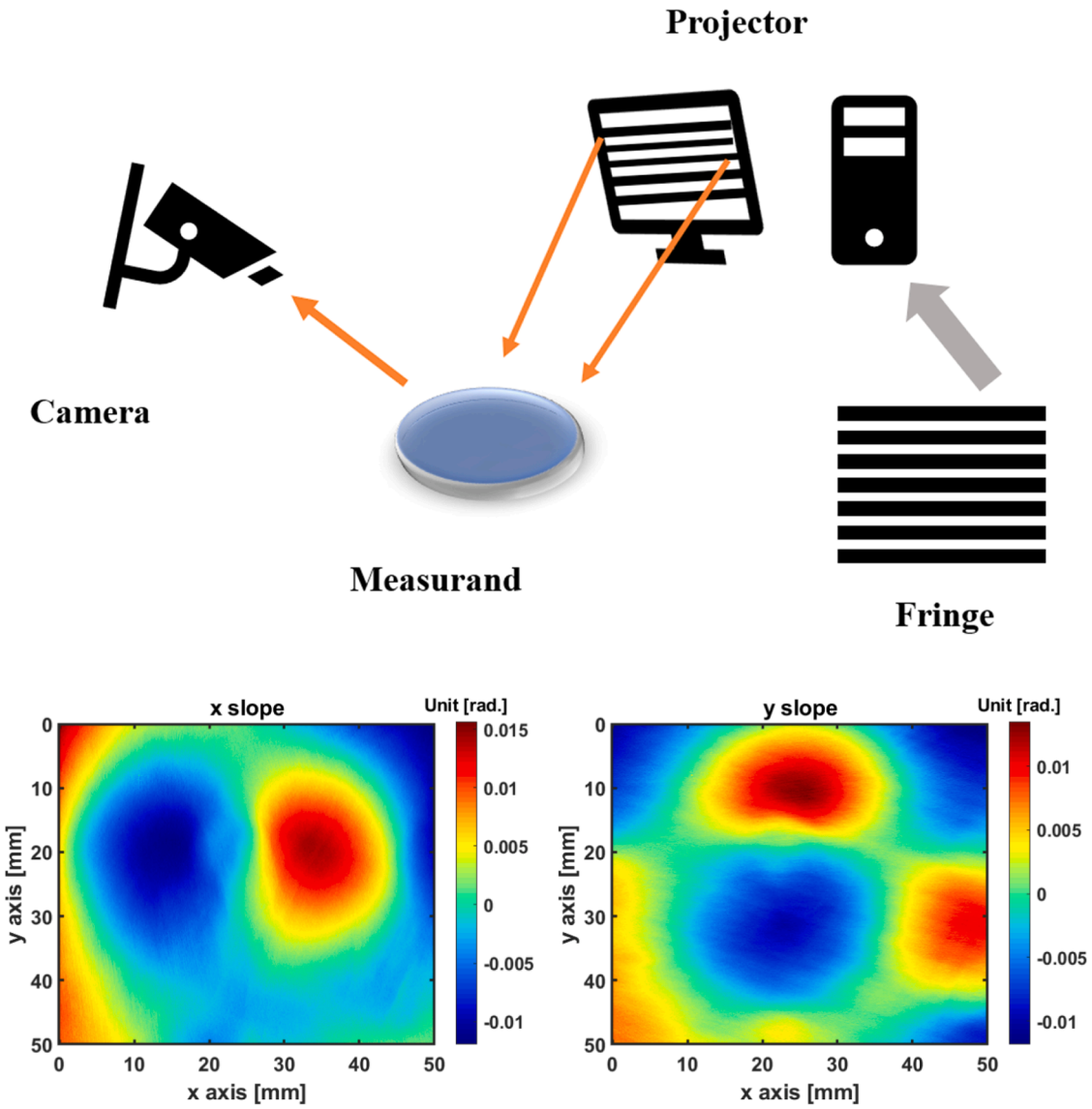

Fig. 18. The principles of deflectometry and its measurement output.

the peak position area in Fig. 19(a) compared to previous algorithm in Fig. 19(b). The initial input of deformable mirror was 72 μm and our proposed method obtained 71.8 μm in the results of peak position while Linh algorithm gave 70.09 μm. This proves that our technique can deal with the high order wavefront retrieval problem, especially in the peak position area.

4. Conclusions and discussion

The principle of a novel and very simple wavefront reconstruction technique that can be integrated with existing algorithms to effectively eliminate error peaks during high-order wavefront retrieval processes was presented in this paper. In order to achieve higher accuracy, a specific wavefront was utilized as a carrier wavefront for reconstruction. This carrier wavefront has stable error, which can neutralize the error peaks of high order aberration wavefronts. A detailed flow chart of the proposed process is also given. Numerous numerical simulations were conducted to demonstrate and assess the performance of the algorithm in terms of speed and accuracy. The outcomes surpassed those of prior algorithms when reconstructing high order aberrations, but the disadvantage is that it requires additional processing time because of the extra steps involved. Experimental comparisons were also performed to confirm the capabilities of our approach.

As mentioned above, the algorithm's lower speed is a disadvantage of this study, since adding steps always increases processing time, but the results clearly indicate that our proposed method can eliminate wavefront error peaks very efficiently.

CRediT authorship contribution statement

Vu-Hai-Linh Nguyen: Writing – original draft, Visualization, Software, Methodology, Data curation, Conceptualization. **Manh-The Nguyen:** Software, Formal analysis, Data curation, Conceptualization. **Hyug-Gyo Rhee:** Writing – review & editing, Supervision, Resources, Project administration, Methodology, Investigation, Funding acquisition, Conceptualization. **Young-Sik Ghim:** Writing – review & editing, Visualization, Validation, Methodology, Conceptualization.

Declaration of competing interest

● All authors have participated in (a) conception and design, or analysis and interpretation of the data; (b) drafting the article or revising

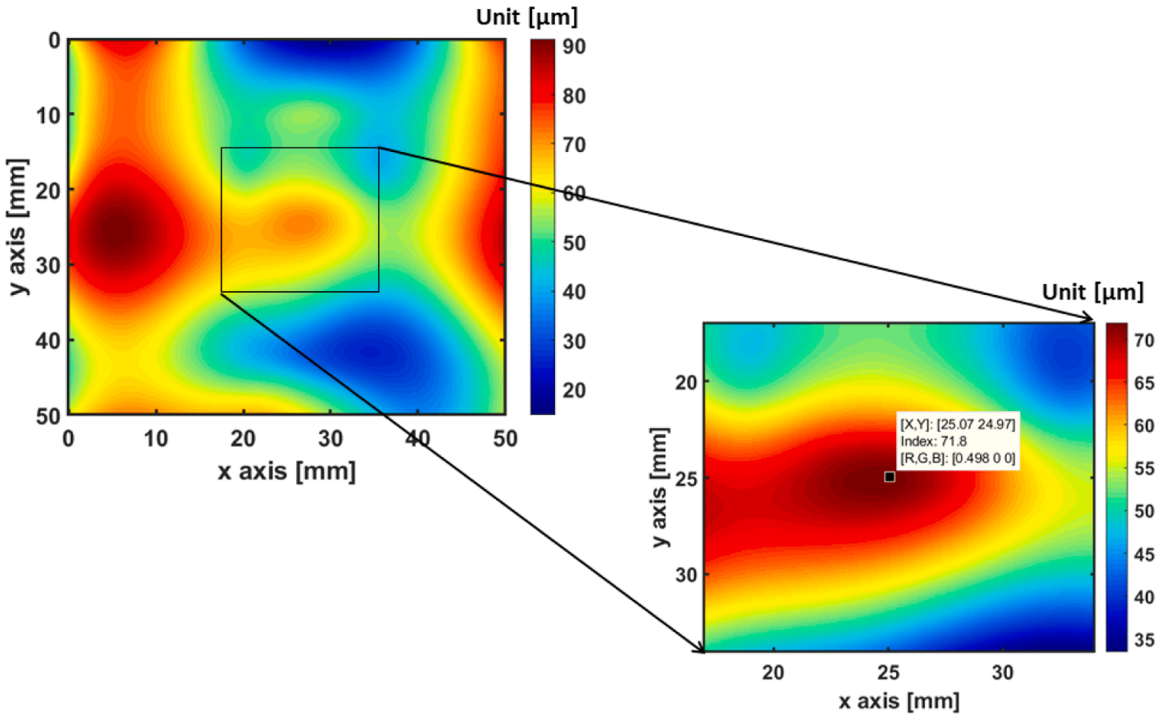

(a)

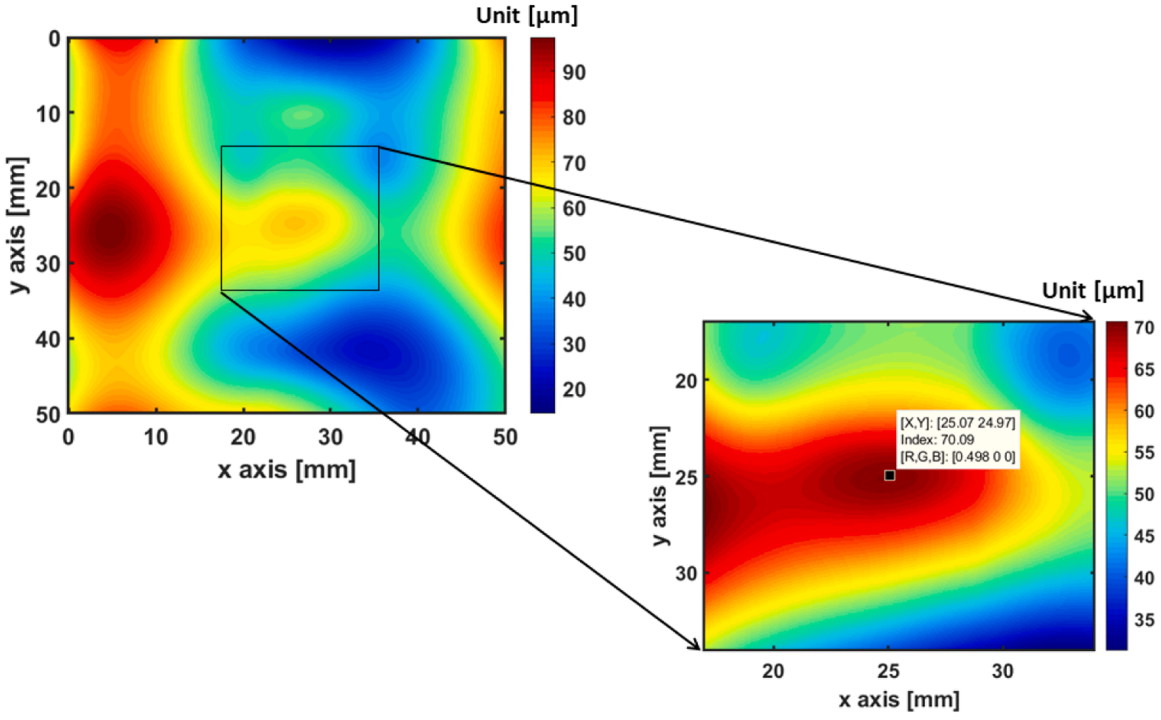

(b)

Fig. 19. Experimental results of deflectometry system with a) Proposed algorithm. (b) Linh algorithm.

it critically for important intellectual content; and (c) approval of the final version.

● This manuscript has not been submitted to, nor is under review at, another journal or other publishing venue.

● The authors have no affiliation with any organization with a direct or indirect financial interest in the subject matter discussed in the manuscript

Data availability

No data was used for the research described in the article.

Acknowledgements

This work was supported in part by the Technology Innovation Program ("RS-2023–00237714″, Development of Dynamic Metrology Tool for CMP Process Stabilization) funded By the Ministry of Trade, Industry & Energy (MOTIE, Korea)(1415187786) and in part by the Technology Innovation Program (20020311, Optical Technology for the Automatic Analysis of EUV Mask) funded by the Ministry of Trade, Industry & Energy (MOTIE, Korea).

References

[1] Avino S, et al. High sensitivity adaptive optics control of laser beam based on interferometric phase-front detection. Opt. Lasers Eng. 2007;45(4):468–70. https://doi.org/10.1016/j.optlaseng.2005.07.013.
[2] Fernández EJ, Iglesias I, Artal P. Closed-loop adaptive optics in the human eye. Opt Lett 2001;26(10):746–8. https://doi.org/10.1364/OL.26.000746.
[3] Wu X, Huang L, Gu N, Tian H, Wei W. Study of a Shack-Hartmann wavefront sensor with adjustable spatial sampling based on spherical reference wave. Opt. Lasers Eng. 2023;160:107289. https://doi.org/10.1016/j.optlaseng.2022.107289.
[4] Riesgo FG, et al. Comparative study of Shack-Hartmann configurations for atmospheric turbulence reconstructions in solar adaptive optics. Opt. Lasers Eng. 2022;158:107157. https://doi.org/10.1016/j.optlaseng.2022.107157.
[5] Ghim YS, Rhee HG, Davies A, Yang HS, Lee YW. 3D surface mapping of freeform optics using wavelength scanning lateral shearing interferometry. Opt. Express 2014;22(5):5098–105. https://doi.org/10.1364/OE.22.005098.
[6] Nguyen MT, Kang P, Ghim YS, Rhee HG. Nonlinearity response correction in phase-shifting deflectometry. Meas Sci Technol 2018;29(4):45012. https://doi.org/10.1088/1361-6501/aaa3ad.
[7] Nguyen MT, Ghim YS, Rhee HG. One-shot deflectometry for high-speed inline inspection of specular quasi-plane surfaces. Opt. Lasers Eng. 2021;147:106728. https://doi.org/10.1016/j.optlaseng.2021.106728.
[8] Saunders JB. Measurement of wave fronts without a reference standard: part 1. The wave-front-shearing interferometer. Measurement 1961;65(4).
[9] Southwell WH. Wave-front estimation from wave-front slope measurements. J Opt Soc Am 1980;70(8):998–1006. https://doi.org/10.1364/JOSA.70.000998.
[10] Shengyang H, Yu N, Fengjie X, Zongfu J. Modal wavefront reconstruction with Zernike polynomials and eigenfunctions of Laplacian. Opt Commun 2013;288:7–12. https://doi.org/10.1016/j.optcom.2012.09.067.
[11] Kewei E, Zhang C, Li M, Xiong Z, Li D. Wavefront reconstruction algorithm based on Legendre polynomials for radial shearing interferometry over a square area and error analysis. Opt. Express 2015;23(16):20267–79. https://doi.org/10.1364/OE.23.020267.
[12] Fried DL. Least-square fitting a wave-front distortion estimate to an array of phase-difference measurements. J Opt Soc Am 1977;67(3):370–5. https://doi.org/10.1364/JOSA.67.000370.
[13] Hudgin RH. Wave-front reconstruction for compensated imaging. J Opt Soc Am 1977;67(3):375–8. https://doi.org/10.1364/JOSA.67.000375.
[14] Huang L, Xue J, Gao B, Zuo C, Idir M. Spline based least squares integration for two-dimensional shape or wavefront reconstruction. Opt. Lasers Eng. 2017;91:221–6. https://doi.org/10.1016/j.optlaseng.2016.12.004.
[15] Zou W, Rolland JP. Quantifications of error propagation in slope-based wavefront estimations. J Opt Soc Am A 2006;23(10):2629–38. https://doi.org/10.1364/JOSAA.23.002629.
[16] Li G, Li Y, Liu K, Ma X, Wang H. Improving wavefront reconstruction accuracy by using integration equations with higher-order truncation errors in the Southwell geometry. J Opt Soc Am A 2013;30(7):1448–59. https://doi.org/10.1364/JOSAA.30.001448.
[17] Nguyen VHL, Rhee HG, Ghim YS. Improved iterative method for wavefront reconstruction from derivatives in grid geometry. Curr. Opt. Photonics 2022;6(1):1–9 [Online]. Available: https://opg.optica.org/copp/abstract.cfm?URI=copp-6-1-1.
[18] Zhong H, Li Y, Qin P, He F, Liu K. Hybrid wavefront reconstruction from multi-directional slope and full curvature measurements using integral equations with higher-order truncation errors for wavefront sensors. Opt. Lasers Eng. 2022;154:106991. https://doi.org/10.1016/j.optlaseng.2022.106991.
[19] Pathak B, Boruah BR. Improved wavefront reconstruction algorithm for Shack–Hartmann type wavefront sensors. J Opt 2014;16(5):55403. https://doi.org/10.1088/2040-8978/16/5/055403.
[20] Phuc PH, Manh NT, Rhee HG, Ghim YS, Yang HS, Lee YW. Improved wavefront reconstruction algorithm from slope measurements. J Korean Phys Soc 2017;70(5):469–74. https://doi.org/10.3938/jkps.70.469.
[21] Hernández-Delgado J, Malacara-Hernández Z, Malacara-Doblado D, Vázquez-Dorrío B, Malacara-Hernández D. Local curvatures and its measurements of an optical surface or a wavefront: a review. Opt Eng 2022;61(5):50901. https://doi.org/10.1117/1.OE.61.5.050901.
[22] Saad Y, van der Vorst HA. Iterative solution of linear systems in the 20th century. J Comput Appl Math 2000;123(1):1–33. https://doi.org/10.1016/S0377-0427(00)00412-X.
[23] Noll RJ. Zernike polynomials and atmospheric turbulence. J Opt Soc Am 1976;66(3):207–11. https://doi.org/10.1364/JOSA.66.000207.
[24] Lakshminarayanan V, Fleck A. Zernike polynomials: a guide. J Mod Opt 2011;58(18):1678. https://doi.org/10.1080/09500340.2011.633763. Oct.